ACS APPLIED MATERIALS & INTERFACES

Research Article

www.acsami.org

CaF_2-Based Near-Infrared Photocatalyst Using the Multifunctional $CaTiO_3$ Precursors as the Calcium Source

Shouqiang Huang,[†] Shengjuan Guo,[‡] Qingji Wang,[‡] Nanwen Zhu,[†] Ziyang Lou,[†] Liang Li,*[,†] Aidang Shan,[†] and Haiping Yuan[†]

[†]School of Environmental Science and Engineering, Shanghai Jiao Tong University, 800 Dongchuan Road, Shanghai, 200240, People's Republic of China

[‡]Daqing Oilfield Engineering Co., Ltd., CNPC, 46 Xiyuan Road, Daqing, Heilongjiang 163712, People's Republic of China

Supporting Information

ABSTRACT: Multistage formation of fluoride upconversion agents from the related-semiconductor precursors provides a promising route for the fabrication of near-infrared (NIR) photocatalysts with high photocatalytic activities. Herein, the cotton templated $CaTiO_3$ "semiconduction" precursors (C-$CaTiO_3$) were used to synthesize the NIR photocatalyst of $Er^{3+}/Tm^{3+}/Yb^{3+}-(CaTiO_3/CaF_2/TiO_2)$ (C-ETYCCT), and the functions of the Ca^{2+} source for CaF_2 and the heterostructure formations were displayed by C-$CaTiO_3$. The generated CaF_2 acted as the host material for the lanthanide ions, and the heterostructures were constructed among anatase, rutile, and the remaining $CaTiO_3$. The induced oxygen vacancies and Ti^{3+} ions enabled the samples to utilize most of the upconversion luminescence for photocatalysis. The NIR driven degradation rate of methyl orange (MO) over C-ETYCCT reached 52.34%, which was 1.6 and 2.5 times higher than those of $Er^{3+}/Tm^{3+}/Yb^{3+}-(CaTiO_3/TiO_2)$ (C-ETYCT) and $Er^{3+}/Tm^{3+}/Yb^{3+}-(CaTiO_3/CaF_2)$ (C-ETYCC), respectively. The degradation rates of MO and salicylic acid over C-ETYCCT with UV−vis−NIR light irradiation were also much higher than those of other samples, which were mainly results of the contributions of its high upconversion luminescence and the efficient electron−hole pair separation.

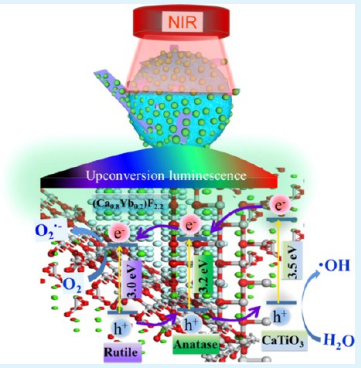

KEYWORDS: *photocatalyst, upconversion, near-infrared light, $CaTiO_3$ precursors, heterostructure*

1. INTRODUCTION

Upconversion agent-assisted photocatalysts are attractive materials for the utilization of near-infrared (NIR) light energy included in sunlight. Lanthanide-doped fluorides exhibit high upconversion efficiencies, and are commonly coupled with semiconductors (i.e., TiO_2,[1,2] ZnO,[3] or CdS[4]) to form the NIR photocatalysts. In the fabrication processes of these NIR photocatalysts, the lanthanide-doped fluorides, that is, $NaYF_4$:Yb,Tm[1−4] and YF_3:Yb,Tm[5,6] were initially prepared and then coated by the semiconductor nanoparticles. According to the reported low degradation rates of dye contaminants,[1−6] these NIR photocatalysts have not yet displayed their maximum photocatalytic abilities, which are subject to the barrier of charge transport properties. Thus, the heterostructures were introduced into NIR photocatalysts to improve the charge carrier separation. The heterostructures of TiO_2/CdS[7] and $TiO_2/CdSe$[8] have been reported for the NIR photocatalysts, where the corresponding photocatalytic activities are much improved compared to those of the samples constructed only by a single semiconductor. Considering the demands of fluoride upconversion agent and heterostructure, a multistage formation method has been found by our group through the fluoride-element contained semiconductor precursors. For example, the $CaWO_4$ precursor, which could display the functions of heterostructure and the Ca^{2+} resource for the $CaWO_4-TiO_2-CaF_2$-based NIR photocatalyst.[9] It should be pointed out that the Ca-containing semiconductor precursors are very flexible for the NIR photocatalysts consisting of CaF_2 and TiO_2, and other favorable properties can be induced into the semiconductor precursors to further increase the photocatalytic activities.

To achieve excellent photocatalytic activity on the CaF_2 and TiO_2 based NIR photocatalyst, we chose a new Ca-containing semiconductor——$CaTiO_3$. $CaTiO_3$ is an *n*-type semiconductor with a band gap energy of about 3.5 eV,[10] and it usually exhibits photoactivity under UV light irradiation.[11] The preobtained $CaTiO_3$ precursors are primarily used as the Ca^{2+} source for the fabrication of $Er^{3+}/Tm^{3+}/Yb^{3+}$ doped CaF_2, and the remaining part after reaction will form heterostructure with TiO_2. Moreover, the cotton fiber template and the anatase/rutile heterostructure are also introduced into the $CaTiO_3$ precursors. The cotton templated morphology in the subsequent NIR photocatalysts can be kept and the light capture efficiency will be improved due to the biometric structure.[12,13]

Received: June 22, 2015
Accepted: August 25, 2015
Published: August 25, 2015

DOI: 10.1021/acsami.5b05557
ACS Appl. Mater. Interfaces 2015, 7, 20170−20178

Scheme 1. Schematic Illustration for the Multi-Stage Fabrication of C-ETYCCT

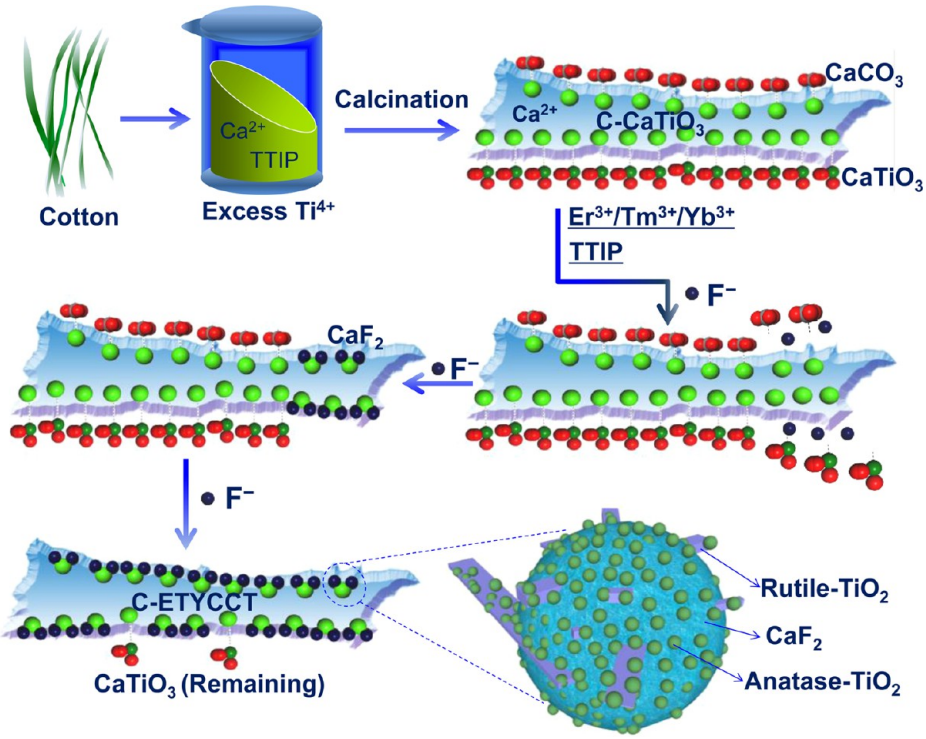

According to the Ti/Ca molar ratio in $CaTiO_3$, excess Ti content is added in the preparation of the cotton templated $CaTiO_3$ precursors (C-$CaTiO_3$). By controlling the calcination process, part of rutile phase will be obtained. Therefore, the heterostructures among $CaTiO_3$, anatase, and rutile are put forward to construct in C-$CaTiO_3$, which will maximize the electron−hole pair separation efficiency for the final obtained NIR photocatalysts.

In this work, C-$CaTiO_3$ included a small part of anatase/rutile phases was initially prepared. Following the addition of $Er^{3+}/Tm^{3+}/Yb^{3+}$ ions and titanium isopropoxide (TTIP, 98%), a series of NIR photocatalysts of $Er^{3+}/Tm^{3+}_{(0.5-8.0\%)}/Yb^{3+}-(CaTiO_3/CaF_2/TiO_{2(15-30\%)})$ ($C\text{-}ET_{(0.5-8.0\%)}YCCT_{(15-30\%)}$) with different TiO_2 contents and Tm^{3+} concentrations were synthesized. Through the comparison of upconversion properties, the optimum contents (15% TiO_2, 0.5% Tm^{3+}) of C-ETYCCT were obtained. On the basis of optimum contents, $Er^{3+}/Tm^{3+}/Yb^{3+}-CaTiO_3$ (C-ETYC), $Er^{3+}/Tm^{3+}/Yb^{3+}-(CaTiO_3/TiO_2)$ (C-ETYCT), and $Er^{3+}/Tm^{3+}/Yb^{3+}-(CaTiO_3/CaF_2)$ (C-ETYCC) were also prepared. The structures, morphologies, and light properties of the samples were characterized by various methods. We investigated the degradations of methyl orange (MO), salicylic acid (SA), and dye wastewater to evaluate the photocatalytic activities of the samples.

2. EXPERIMENTAL SECTION

2.1. Chemicals and materials. $Er(NO_3)_3{\cdot}5H_2O$, $Tm(NO_3)_3{\cdot}5H_2O$, $Yb(NO_3)_3{\cdot}5H_2O$, $Ca(NO_3)_2{\cdot}4H_2O$, TTIP, and cotton fibers were used as received without further purification.

2.2. Preparation of C-$CaTiO_3$. $Ca(NO_3)_2{\cdot}4H_2O$ (0.048 mol) was dissolved in 50 mL distilled water, followed by the addition of 100 mL absolute ethanol. The pH of the solution was adjusted to 1 by adding nitric acid, and then 0.05 mol of TTIP was introduced into the above solution. After the solution was stirred for 30 min, 5 g of cotton fibers was added into the resultant clear solution. The obtained mixture was placed in a thermostat water bath operating at 80 °C for 6 h. The precipitates via centrifugation and drying were calcined in air at 500 °C for 4 h to form C-$CaTiO_3$ (Scheme 1). The heating rate was set to 2 °C/min to ensure the slow removal of the cotton fibers.

2.3. Preparation of C-ETYCCT Sample. In a typical procedure of C-ETYCCT, C-$CaTiO_3$ (0.5 g), $Er(NO_3)_3{\cdot}5H_2O$, $Tm(NO_3)_3{\cdot}5H_2O$, and $Yb(NO_3)_3{\cdot}5H_2O$ were added into 40 mL of distilled water and totally dispersed by ultrasonication for 2 min, and the pH of the mixture was adjusted to 1 by adding nitric acid. Then, 20 mL of absolute ethanol containing TTIP was added into the mixture under continuous stirring. The molar ratio of Ca^{2+}/Ti^{4+} (TTIP)/$Yb^{3+}/Er^{3+}/Tm^{3+}$ was 100:15:20:1:0.5%. After stirring for 30 min, 40 mL of NaF solution (molar ratio of Ca^{2+}/F^- = 1:5) was added dropwise into the above mixture. The resultant mixture was kept at 80 °C via a thermostat water bath for 8 h. The precipitates were separated through centrifugation with distilled water and ethanol, and dried at 60 °C for 12 h. The obtained powders were calcined at 500 °C for 4 h to form the C-ETYCCT samples (Scheme 1). Other samples of $C\text{-}ET_{(0.5-8.0\%)}YCCT_{30\%}$ with different TiO_2 content (30%) and Tm^{3+} concentrations (0.5, 1.0, 3.0, 5.0, and 8.0%), and C-ETYC, C-ETYCT, and C-ETYCC were synthesized following the same procedures mentioned above.

2.4. Characterization. The crystalline phases of the samples were measured by X-ray power diffraction analysis (XRD, Bruker D8 Advance X-ray Diffractometer) at 40 kV and 40 mA using Cu K_α radiation (λ = 1.5406 Å). The microstructures were observed by using the Sirion 200 field emission scanning electron microscope (FESEM) and the JEM-2100F transmission electron microscope (TEM), and the elemental composition was determined by the INCA X-Act energy-dispersive spectroscopy (EDS) instrument installed on Sirion 200 FESEM. The surface chemistry was studied by the X-ray photoelectron spectroscopy (XPS, Kratos Axis Ultra^{DLD}), and the binding energies of adventitious carbon (284.8 eV) were used for charge correction. The light absorption spectra were collected on the Lambda 750 UV−vis−NIR spectrophotometer. Upconversion luminescence spectra were recorded by exciting samples with a 980 nm semiconductor solid laser. Upconversion decay lifetimes were measured under the excitation of 953.6 nm Raman laser with 10 ns pulse width. The electron spin

DOI: 10.1021/acsami.5b05557
ACS Appl. Mater. Interfaces 2015, 7, 20170−20178

resonance (ESR) spectra were measured using an EMX-8 ESR spectrometer (Bruker BioSpin Corp.) at a microwave power of 5 mW.

2.5. Photocatalytic Activities. The photocatalytic activities of the samples were evaluated by the degradation of MO and SA under NIR ($\lambda \geq 780$ nm) and UV−vis−NIR irradiations provided by a 1000 W high pressure mercury lamp or a 500 W Xe lamp. Typically, 20 mg of the samples were dispersed in 20 mL of MO or SA aqueous solutions (10 mg/L). Prior to irradiation, the suspensions were magnetically stirred in the dark for 2 h to attain adsorption/desorption equilibrium. Every periodic interval, 2.0 mL of the suspensions were collected and analyzed by a UV−vis spectrophotometer (Hitachi U-3900). In the photoactivity test for ●OH radical generation, terephthalic acid (TA, 4×10^{-4} M in a 2×10^{-3} M NaOH solution) was used, and the test methods were similar to those mentioned above for the MO and SA degradations. The dye wastewater was further used to test the photocatalytic activity of C-ETYCCT under UV−vis−NIR irradiation provided by the high pressure mercury lamp, where the initial total organic carbon (COD) was 2350 mg/L. The degraded dye wastewater samples were characterized by fluorescence excitation−emission matrix (EEM) spectroscopy (F-7000, Hitachi). Scanning emission spectra were obtained from 250 to 595 nm by varying the excitation wavelength from 220 to 500 nm at 5 nm increments. Then, the obtained dye wastewater samples were diluted 25 times for the total organic carbon (TOC, multi N/C 3100 analyzer) and chemical oxygen demand (COD, potassium dichromate method) measurements.

3. RESULTS AND DISCUSSION

3.1. XRD Analysis. The crystal structures of C-$CaTiO_3$, C-ETYCT, C-ETYCC, and C-ETYCCT were characterized by XRD (Figure 1). The XRD pattern of C-$CaTiO_3$ (Figure 1a)

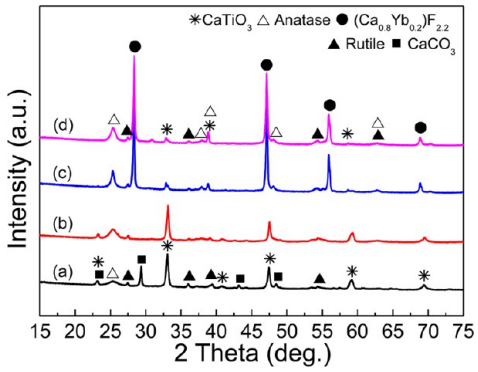

Figure 1. XRD patterns of (a) C-$CaTiO_3$, (b) C-ETYCT, (c) C-ETYCC, and (d) C-ETYCCT.

exists a small amount of anatase (JCPDS Card No. 89-4203), rutile (JCPDS Card No. 89-4202), and $CaCO_3$ (JCPDS Card No. 72-1214), in addition to the main phase of $CaTiO_3$. The diffraction peaks at 33.04, 47.44, 59.20, and 69.43° are assigned to the (112), (220), (312), and (224) planes of $CaTiO_3$ (JCPDS Card No. 78−1013), respectively. The phase compositions through the Jade reference data of $CaTiO_3$, anatase, rutile, and $CaCO_3$ are 59.7, 5.0, 4.8, and 30.5%, respectively. $CaCO_3$ is bound to form via the reaction between the Ca-contained oxides and the CO_2 gas caused by the burning of cotton fibers. After the synthesis of C-ETYCT (Figure 1b), the phases of $CaTiO_3$ (77.3%), anatase (16.0%), and rutile (6.7%) are kept, while the $CaCO_3$ phase is disappeared. It is attributed to the decomposition of $CaCO_3$ in the acid mixture containing TTIP (pH = 1), which results in the increased $CaTiO_3$ content for C-ETYCT. Figure 1c shows the XRD pattern of C-ETYCC, and four crystal phases of $(Ca_{0.8}Yb_{0.2})F_{2.2}$ (JCPDS Card No. 87-0976), $CaTiO_3$, anatase, and rutile are detected. With the addition of F^- ions, the Ca^{2+} ions in $CaTiO_3$ and $CaCO_3$ can be released to generate CaF_2, and the remaining $CaTiO_3$ will form heterostructures with anatase and rutile (Scheme 1). Importantly, the CaF_2 phase is present in the form of $(Ca_{0.8}Yb_{0.2})F_{2.2}$, suggesting the Yb^{3+} ions have been doped into CaF_2. The Er^{3+} and Tm^{3+} related phases are not detected due to their very small content. In comparison to C-ETYCC, the diffraction peaks of C-ETYCCT have been broadened slightly owing to the added TiO_2 nanocrystals derived from TTIP, which are beneficial for the improvement of photocatalytic activities.

3.2. Morphologies and Microstructures of the Samples. The morphologies of the samples are observed by SEM (Figure S1) and TEM (Figure 2). As shown in Figure S1a and Figure 2a, C-$CaTiO_3$ possesses the strip-like morphology of cotton fibers, which is constructed by the $CaTiO_3$, anatase, rutile, and $CaCO_3$ particles (Figure 2b) mentioned in the XRD pattern (Figure 1a). After the introduction of F^- ions, many spherical particles with an average size of 200 nm clearly appear on the surface of the strip-like morphology in C-ETYCC (Figure S1b). For C-ETYCCT, the strip-like morphology is kept (Figure S1c), and its surface is filled with numerous small particles (Figure S 1d). From the TEM image of these small particles (Figure 2c), it can be observed many spherical particles with a size of 200 nm are included, and the surfaces of them are deposited with many nanoparticles and nanorods (Figure 2d). The selected-area electron diffraction pattern reveals the clear diffraction rings (inset of Figure 2d), which is associated with the polycrystalline nature of the whole spherical particles. According to the high-resolution TEM (HRTEM) image (Figure 2e), it can be inferred that the spherical particle belongs to $(Ca_{0.8}Yb_{0.2})F_{2.2}$, because the detected lattice fringe spacing of 0.32 nm is close to its (111) planes. The Fourier transform electron diffraction pattern of the nanorod confirms the (110) planes of rutile (Figure 2g) and thus indicates that rutile possesses the nanorod morphology. The HRTEM images of the nanoparticles deposited on rutile and $(Ca_{0.8}Yb_{0.2})F_{2.2}$ are shown in Figure 2f,h, and the detected lattice fringe spacing of 0.35 nm is close to the (101) planes of anatase. Thus, the heterostructure of the connected anatase and rutile will facilitate the photogenerated charge carrier separation.

3.3. Component Analysis. The SEM images of C-ETYCCT with low (5 keV) and high (20 keV) voltages are shown in Figure S2a and b, respectively. To determine the elemental distribution, the EDS mapping results are highlighted by the red frames in Figure S2. The elements Ca, Ti, F, Yb, Er, Tm, and O are detected with the atomic ratio of 8.37:9.19:51.41:1.29:0.08:0.05:29.61% (Figure S2c), and all these elements are distributed homogeneously throughout the strip-like structure. The surface chemical composition of C-ETYCCT is detected by XPS, as shown in Figure S3. The survey scan XPS spectrum (Figure S3a) represents the main elements of Ca, Ti, Yb, F, and O. The Ca 2p peaks located at 347.8 and 351.3 eV are in good accordance with Ca $2p_{2/3}$ and Ca $2p_{1/2}$ (Figure S3b), respectively. The Ti 2p spectrum (Figure S3c) exhibits well resolved peaks at 457.8 and 463.4 eV, which correspond to Ti $2p_{3/2}$ and Ti $2p_{1/2}$, respectively. Figure S3d shows the Yb 4d spectrum, and the peaks at 186.1 and 197.5 eV are attributed to Yb $4d_{5/2}$ and Yb $4d_{3/2}$, respectively. On the basis of XPS results, we calculated the atomic ratio of Ca/Ti/Yb to be 13.63:13.32:2.41%, meaning that a large part of the added Yb^{3+} ions are located at the outmost surface of C-ETYCCT, which is beneficial to the NIR light absorption.

DOI: 10.1021/acsami.5b05557
ACS Appl. Mater. Interfaces 2015, 7, 20170−20178

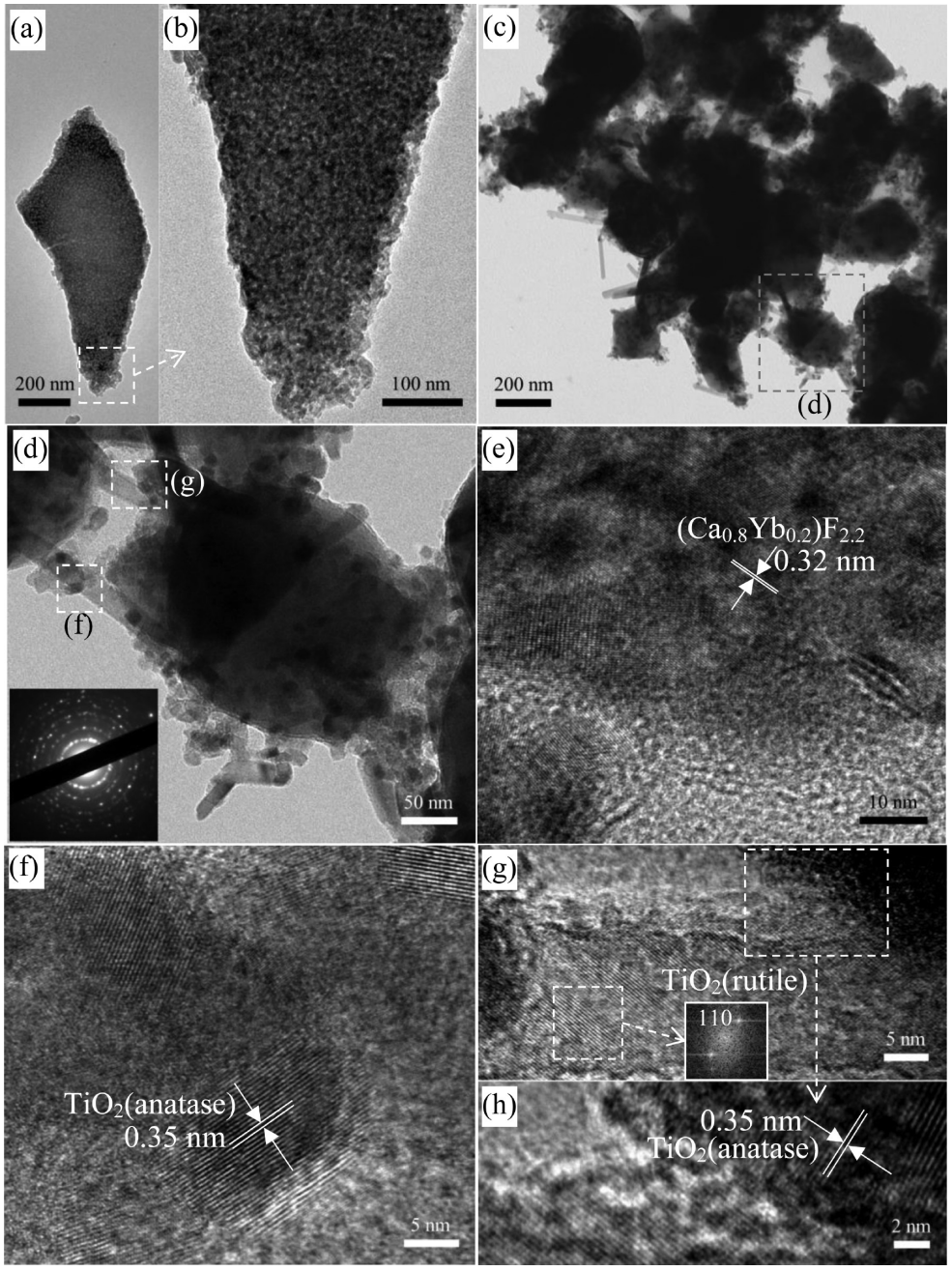

Figure 2. (a and b) TEM images of C-$CaTiO_3$; (c and d) TEM (inset, selected-area electron diffraction pattern) and (e–h) HRTEM images (inset, Fourier transform electron diffraction pattern) of C-ETYCCT.

3.4. Upconversion Luminescence Properties. In the preparation of CaF_2 and TiO_2 based NIR photocatalysts, excess TiO_2 content will weaken the upconversion properties, while too low content will reduce the photocatalytic activities. Meanwhile, the optimum doping concentration of Tm^{3+} ions is also important for the upconversion luminescence. As shown in Figure 3a,c, the upconversion emission intensity of C-$ETYCCT_{15\%}$ (C-ETYCCT) is much stronger than those of C-$ET_{(0.5-8.0\%)}YCCT_{30\%}$ under 980 nm NIR light excitation. Under the same condition, the upconversion emission intensities of C-$ET_{(0.5-8.0\%)}YCCT_{30\%}$ decline gradually with increasing the Tm^{3+} contents from 0.5 to 8.0%. Thus, based on the TiO_2 content of 15% and the Tm^{3+} content of 0.5%, the upconversion properties among C-$CaTiO_3$, C-ETYCT, C-ETYCC, and C-ETYCCT are compared and shown in Figure 3b,d. The emission spectra include the red (652 nm), green (541 and 522 nm), violet (407 nm), and UV (381 nm) light, which result from the $^4F_{9/2} \rightarrow {}^4I_{15/2}$, $^4S_{3/2} \rightarrow {}^4I_{15/2}$, $^2H_{11/2} \rightarrow {}^4I_{15/2}$, $^2H_{9/2} \rightarrow {}^4I_{15/2}$, and $^4G_{11/2} \rightarrow {}^4I_{15/2}$ transitions of Er^{3+} ions,[2] respectively. The blue (485 and 455 nm) and UV (364, 351, and 292 nm) light emissions are assigned to the $^1G_4 \rightarrow {}^3H_6$, $^1D_2 \rightarrow {}^3F_4$, $^1D_2 \rightarrow {}^3H_6$, $^1I_6 \rightarrow {}^3F_4$, and $^1I_6 \rightarrow {}^3H_6$ transitions of Tm^{3+} ions,[1,3] respectively. The $^1G^4 \rightarrow {}^3F_4$ transitions of Tm^{3+} ions can also contribute the 652 nm red emission.[9]

It can be found that the introduced CaF_2 enhances the upconversion luminescence greatly, and the added 15% content of TiO_2 slightly reduces the upconversion emission intensity of C-ETYCCT compared to C-ETYCC. In our previous works, we reported the TiO_2 coatings could improve the upconversion emission intensities for $Er^{3+}/Tm^{3+}/Yb^{3+}$-($CaWO_4/TiO_2/CaF_2$)[9]

DOI: 10.1021/acsami.5b05557
ACS Appl. Mater. Interfaces 2015, 7, 20170–20178

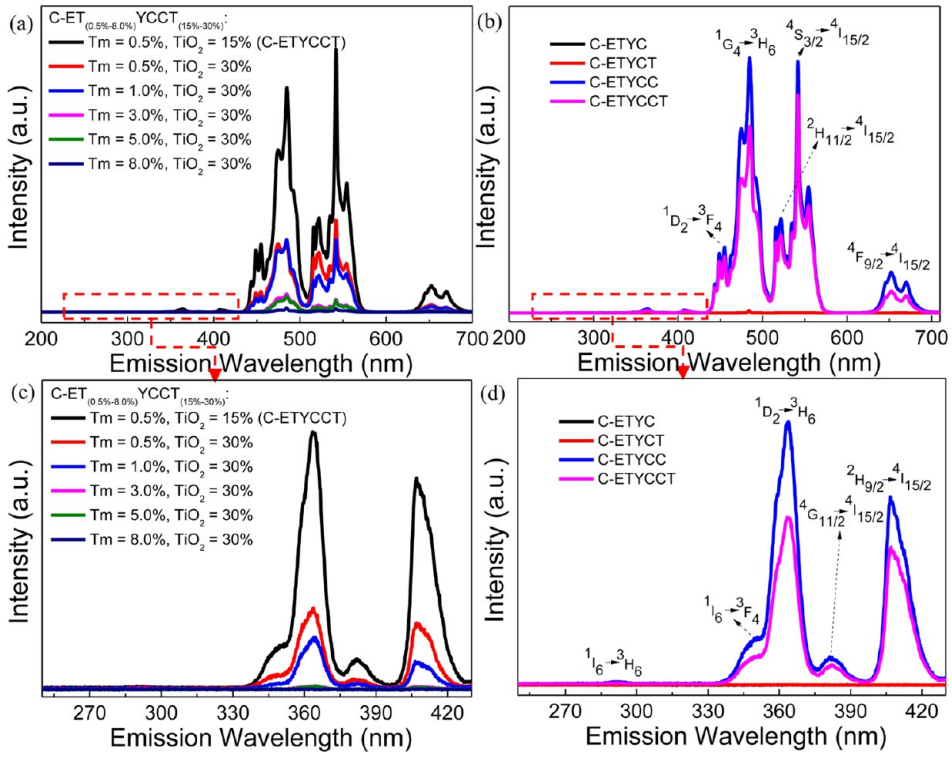

Figure 3. (a and c) Upconversion luminescence spectra of C-ET$_{(0.5-8.0\%)}$YCCT$_{(15-30\%)}$ with different TiO_2 contents and Tm^{3+} concentrations under 980 nm NIR excitation (output current = 3.0 A). (b and d) Upconversion luminescence spectra of C-ETYC, C-ETYCT, C-ETYCC, and C-ETYCCT under 980 nm NIR excitation (output current = 3.0 A).

and $Er^{3+}/Tm^{3+}/Yb^{3+}/Bi^{3+}$-($NaY(WO_4)_2/TiO_2/YF_3$),[14] where their upconversion agents were connected to TiO_2 nanocrystals in the outermost surfaces. The structure of C-ETYCCT is different from them, and the enhanced effect on upconversion luminescence is not exhibited.

The fluorescence decay curves of the $^4S_{3/2}$ (Er^{3+}) and $^1G_4$ (Tm^{3+}) levels are shown in Figure S4a,b. The lifetimes of the $^4S_{3/2}$ levels in C-ETYCC and C-ETYCCT are 41 and 46 μs, respectively, and the small difference is consistent with their comparable green light emissions (Figure 3b). For the $^1G_4$ levels, the lifetime of C-ETYCCT is 39 μs, lower than that (70 μs) of C-ETYCC, resulting in the decreased blue emission intensity for C-ETYCCT compared to C-ETYCC, which may be due to the light-scattering caused by the further induced anatase nanoparticles. In the violet and UV light emissions, the intensities of C-ETYCCT decrease more obvious compared to its blue emission (Figure 3d), and it is owing to the more improved energy transfer process from CaF_2 to TiO_2.

3.5. NIR-Driven Photocatalytic Activities. The NIR driven photocatalytic activities of the samples are investigated using the degradation of MO as a model. Figure 4a shows the peak maxima of MO at 464 nm shift to lower absorbance values over C-ETYCCT as the irradiation time extend, and higher degradation rate of 52.34% is obtained for C-ETYCCT (Figure 4b) compared to C-ETYCT (33.30%) and C-ETYCC (20.95%). Under the sun-like NIR light irradiation (Figure 4c), C-ETYCCT also possesses better photocatalytic activity (24.01%) than those of C-ETYCT (9.92%) and C-ETYCC (9.18%). The C/C_0 conversion plots of MO over C-$CaTiO_3$ are very stable, since there is no upconversion property in C-$CaTiO_3$. As for the C-ET$_{(0.5-8.0\%)}$YCCT$_{30\%}$ samples with higher TiO_2 content (Figure S5 and Table S1), the NIR driven degradation rates are decreased gradually as the Tm^{3+} contents increased, which are ascribed to the weakened upconversion emissions caused by the concentration quenching effect of Tm^{3+} ions (Figure 3a,c). Thus, it can be inferred that the NIR driven photocatalytic activities of the samples are mainly dependent on their upconversion luminescence, especially the short-wavelength emissions.

The light absorption properties and the electron−hole pair separation efficiencies also display vital roles for the improvement of photocatalytic activities. The UV−vis−NIR diffuse reflectance spectra of the samples are shown in Figure S6. C-ETYCCT and C-ETYCT possess stronger UV light absorption intensities compared to C-$CaTiO_3$ and C-ETYCC, due to their higher TiO_2 contents added in the fabrication process. Conversely, C-$CaTiO_3$ exhibits stronger visible light absorption ability compared to C-ETYCCT and C-ETYCT, and it is associated with its crystal defects and oxygen vacancies. Figure 4d shows the ESR spectra for C-$CaTiO_3$, C-ETYCT, C-ETYCC, and C-ETYCCT. There are many ESR signals included in C-$CaTiO_3$, such as O_2^{3-} (g = 2.0317),[15] ionic superoxide anion O_2^- (g = 2.0267),[16] $\bullet O_2^-$ (g = 2.0063),[17] and single electron oxygen vacancy $V_o^\bullet$ (g = 2.0038, 1.9868, and 1.9820).[18−21] The ESR signals of C-ETYCT locate at g = 2.0020 and 1.9721, which correspond to $V_o^\bullet$ and Ti^{3+},[19−21] respectively. C-ETYCC and C-ETYCCT mainly possess the $V_o^\bullet$ signal at g = 2.0020. The detected oxygen vacancies and Ti^{3+} ions enable C-ETYCT to absorb its visible light upconversion emissions.[22] In addition, the visible light absorption property of C-$CaTiO_3$ can also be kept in the obtained C-ETYCC and C-ETYCCT samples, and most of the visible light upconversion emissions can be used by them for photocatalysis.

The photocatalytic mechanism is shown in Figure 5. The NIR light through the filter ($\lambda \geq 780$ nm) excites the

DOI: 10.1021/acsami.5b05557
ACS Appl. Mater. Interfaces 2015, 7, 20170−20178

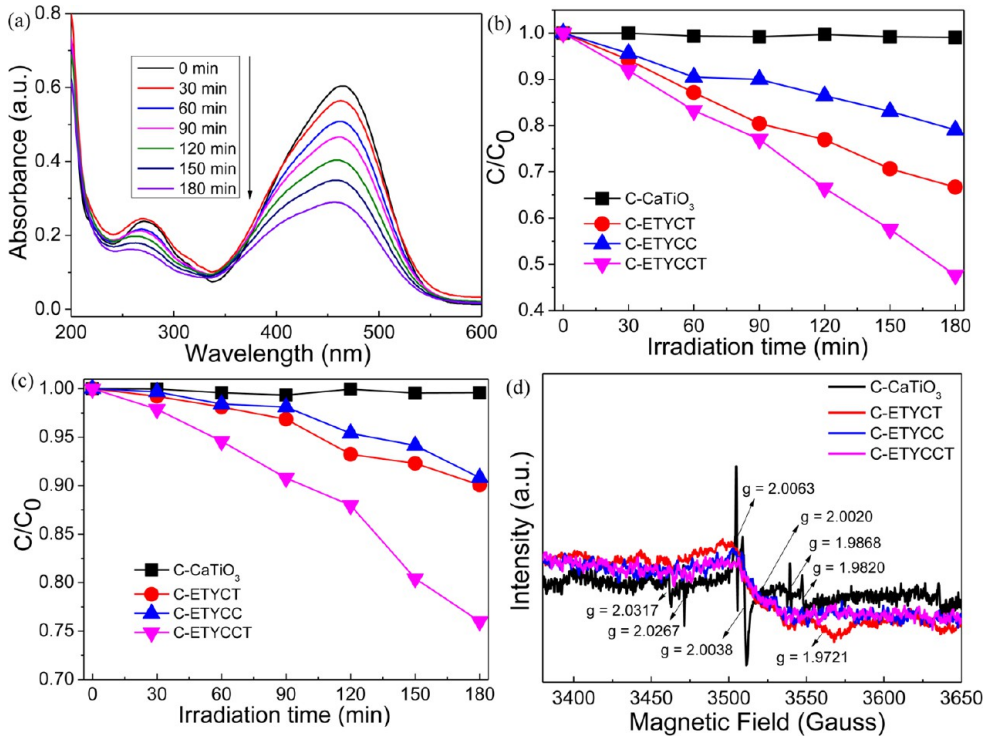

Figure 4. (a) Time-dependent absorption spectra of MO over C-ETYCCT and (b) the C/C_0 conversion plots over the samples under NIR light ($\lambda \geq 780$ nm) irradiation provided by a 1000 W high pressure mercury lamp. (c) C/C_0 conversion plots of MO over the samples under NIR ($\lambda \geq 780$ nm) light irradiation provided by a 500 W Xe lamp. (d) ESR spectra of the samples.

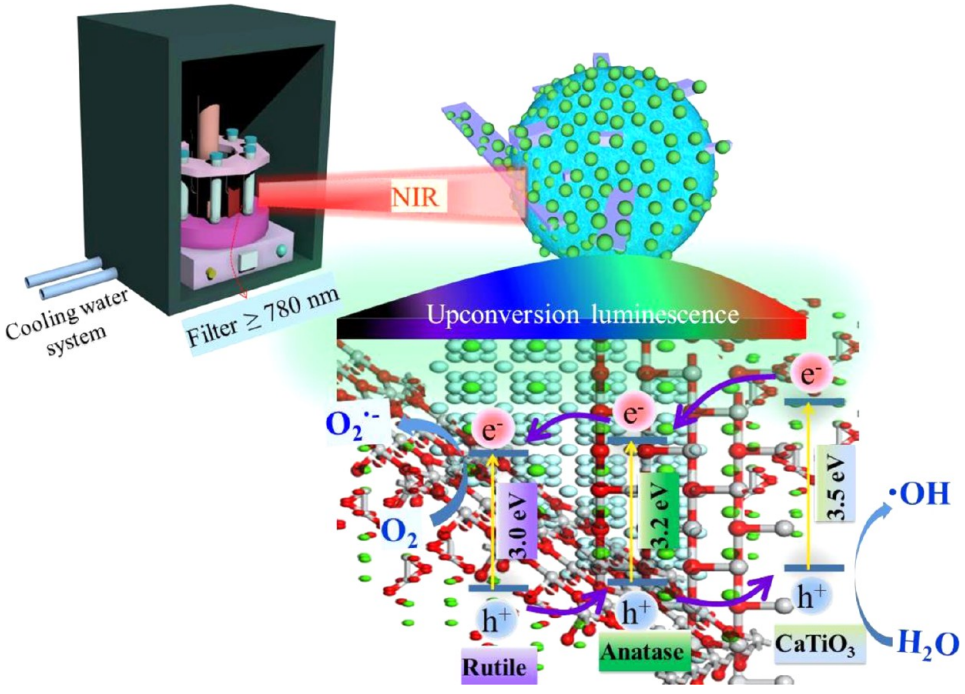

Figure 5. Schematic illustration of energy transfer mechanism for the photocatalytic reaction process over C-ETYCCT under NIR irradiation.

$Er^{3+}/Tm^{3+}/Yb^{3+}-CaF_2$ in C-ETYCCT to produce upconversion luminescence. These upconversion emissions, especially the UV (381, 364, 351, and 292 nm) and violet (407 nm) light can significantly generate the electrons (e^-) and holes (h^+). According to the heterostructures among anatase, rutile, and $CaTiO_3$, the electrons can be transferred from the conduction band (CB) of $CaTiO_3$ to the lower CBs of anatase and rutile. Meanwhile, the holes can be transferred from the valence band (VB) of rutile to the VBs of anatase and $CaTiO_3$, and thus, the charge carrier separation is promoted. As shown in Figure 3b,d, the upconversion luminescence of C-ETYCCT is much stronger than that of C-ETYCT. In the violet and UV emission regions, the intensities of C-ETYCCT also decrease largely compared to those of C-ETYCC. The decay curves of the violet

DOI: 10.1021/acsami.5b05557
ACS Appl. Mater. Interfaces 2015, 7, 20170−20178

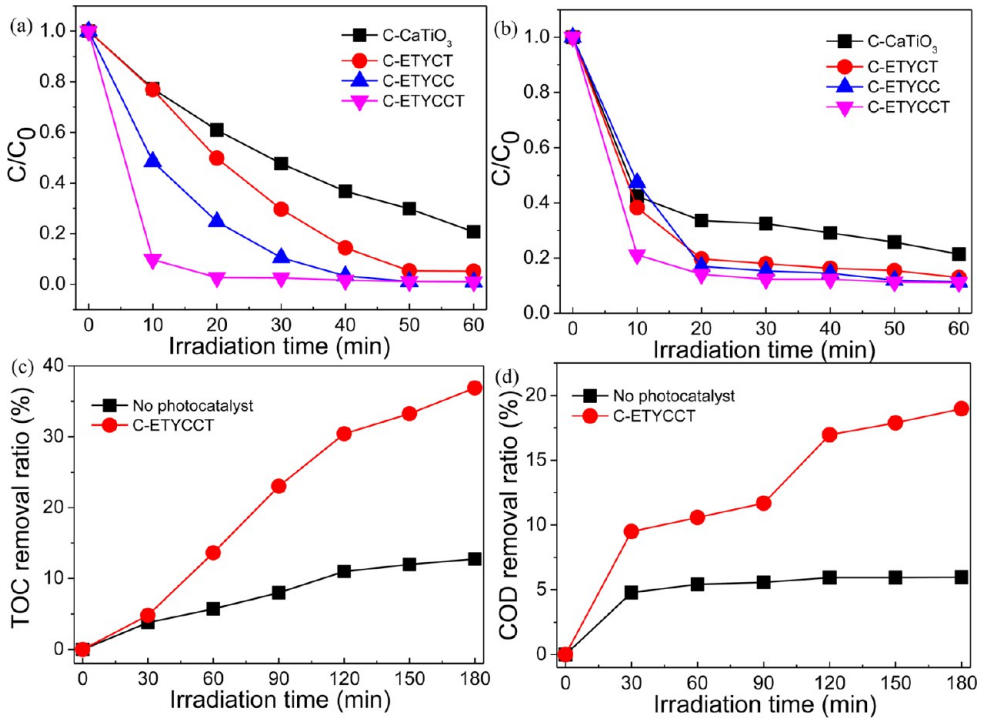

Figure 6. C/C_0 conversion plots of (a) MO and (b) SA over the samples under UV−vis−NIR light irradiation provided by a 1000 W high-pressure mercury lamp. (c) TOC and (d) COD removal rates of the dye wastewater over C-ETYCCT under UV−vis−NIR light irradiation provided by a 1000 W high pressure mercury lamp.

($^2H_{9/2} \rightarrow {}^4I_{15/2}$, Er^{3+}) emission in C-ETYCC and C-ETYCCT are shown in Figure S7. The corresponding lifetime of C-ETYCCT is smaller than that (21 μs) of C-ETYCC, meaning the more effective energy transfer process occurred in C-ETYCCT from the upconversion agent of $Er^{3+}/Tm^{3+}/Yb^{3+}$-CaF_2 to TiO_2. The PL spectra of the samples under 300 nm excitation are shown in Figure S8. The lower PL emission intensity of C-ETYCCT indicates its higher electron−hole pair separation efficiency compared to C-ETYCC. C-ETYCT possesses the lowest emission intensity, while its upconversion luminescence is weakest among the samples. Therefore, benefitting from the above advantages, C-ETYCCT exhibits the best NIR driven photocatalytic activities compared to C-ETYCC and C-ETYCT. The degradation rate (52.34%) of MO over C-ETYCCT also exceeds the reported value (46.57%) of $Er^{3+}/Tm^{3+}/Yb^{3+}$ tridoped ($CaWO_4/TiO_2/CaF_2$),[9] which demonstrates the advantage of the multifunctional semiconductor precursors for the improvement of photocatalytic activities. From the C/C_0 conversion plots of MO in Figure 4b, it can be found that C-ETYCT has a higher degradation rate of 33.30% than that (20.95%) of C-ETYCC. Although C-ETYCT possesses the weakest upconversion luminescence, its short-light absorption property and the electron−hole pair separation efficiency are better than those of C-ETYCC and thus display better photocatalytic activity.

3.6. UV−Vis−NIR-Driven Photocatalytic Activities. The UV−vis−NIR-driven photocatalytic activities of the samples are evaluated by photodegradation of MO and SA. As shown in Figure 6a, in the first degradation of 10 min, the degradation rates of MO over C-$CaTiO_3$, C-ETYCT, C-ETYCC, and C-ETYCCT are 22.73, 23.13, 51.54, and 90.25%, respectively. Meanwhile, the degradation rates of SA are 57.58, 61.71, 52.63, and 78.79% for C-$CaTiO_3$, C-ETYCT, C-ETYCC, and C-ETYCCT (Figure 6b), respectively. With the synergistic effects of the strong upconversion luminescence, high short-wavelength light absorption intensity, and efficient electron−hole pair separation, C-ETYCCT exhibits best photocatalytic activities among the samples. The opposite behaviors between C-ETYCT and C-ETYCC for the MO and SA degradations may be resulted from their selectivities. As the irradiation time extended to 20 min, the degradation rate of SA over C-ETYCC exceeds that of C-ETYCT, indicating its upconversion luminescence starts to display the predominant role. The •OH radicals are considered to be the major species for the dye degradation, and they are detected by terephthalic acid under UV−vis−NIR light irradiation. The •OH trapping fluorescence spectra of the terephthalic acid solution containing C-ETYCCT are shown in Figure S9a, and the emission peaks at 423 nm of the 2-hydroxyterephthalic acid increase steadily as a function of the irradiation time. Figure S9b shows the time-dependent •OH radical yields over the samples, and C-ETYCCT possesses the highest amount, which is responsible for its best photocatalytic activity. It can also be observed that the productive rate of •OH radical yields over C-ETYCC is lower than that of C-ETYCT at the beginning, and then C-ETYCC shows stronger ability in producing •OH radicals, resulting in the degradation rates of SA lower and then higher compared to those of C-ETYCT.

The photocatalytic activity of C-ETYCCT is further evaluated by the degradation of dye wastewater under UV−vis−NIR light irradiation, and the results are shown in Figure 6c,d. In the absence of photocatalysts, a small degradation occurs owing to the provided strong UV light source. With the addition of C-ETYCCT, the TOC and COD removal rates increase significantly, with the values of 36.90 and 18.98%, respectively. The EEM fluorescence spectra of the dye wastewater are shown in Figure 7. Prior to irradiation, there are three fluorescence peaks included in the dye wastewater (Figure 7a). The fluorescence peak of region IV at

DOI: 10.1021/acsami.5b05557
ACS Appl. Mater. Interfaces 2015, 7, 20170−20178

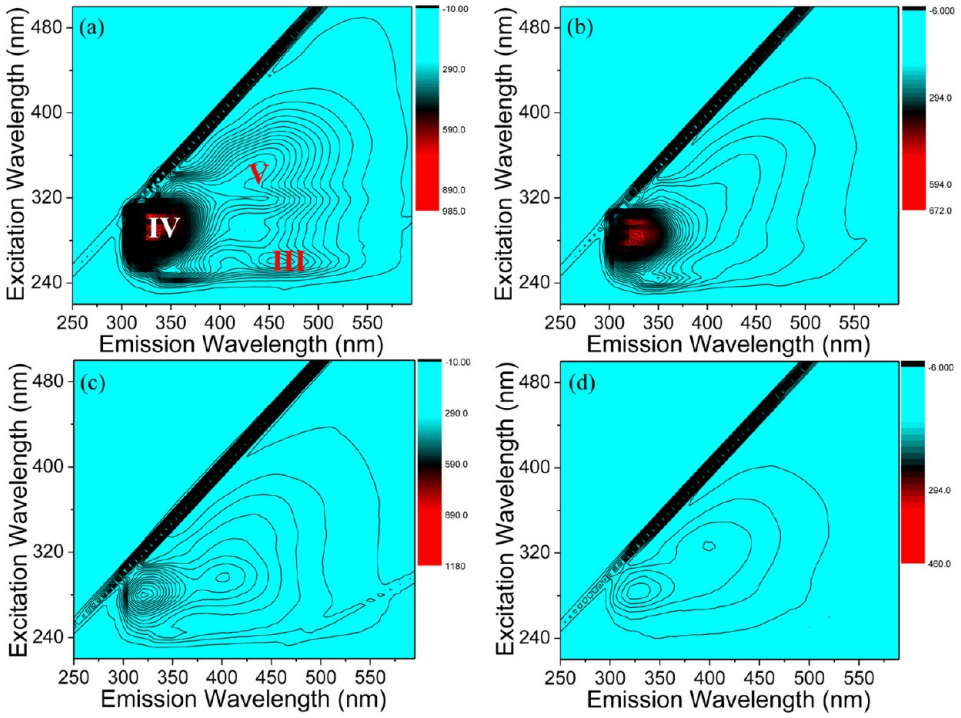

Figure 7. EEM fluorescence spectra of dye wastewater over C-ETYCCT under UV−vis−NIR light irradiation: (a) 0, (b) 30, (c) 120, and (d) 180 min.

excitation wavelengths/emission wavelengths (Ex/Em) of 250−320/300−375 nm is attributed to aromatic-like compounds, such as tryptophan and tyrosine.[23,24] Region III represents fulvic acid-like compounds with Ex/Em of 240−250/440−480 nm. Region V at Ex/Em of 330−400/400−530 nm is related to humic-like compounds. In the first degradation of 30 min (Figure 7b), all the fluorescence peak intensities are decreased, and the fulvic acid-like compounds have already disappeared. As the irradiation time extends to 120 min (Figure 7c), the fluorescence intensity of aromatic-like compounds continue to decrease. Meanwhile, the fluorescence peak of humic-like compounds is shifted to Ex/Em of 295/400 nm, meaning that the macromolecular structures (aromatic ring and alicyclic) of humic-like compounds have been destroyed, and the amounts of carbonyl, hydroxyl and other functional groups are also declined.[25,26] As shown in Figure 7d, the aromatic-like and humic-like compounds can be further degraded as the irradiation time extend to 180 min. Therefore, the degradation results confirm the practical application of C-ETYCCT in the treatment of dye wastewater.

4. CONCLUSIONS

A novel NIR photocatalyst of C-ETYCCT was synthesized by a modified sol−gel method. The C-$CaTiO_3$ precursors were used as the Ca^{2+} source for CaF_2 formation and the heterostructures with anatase and rutile. The obtained C-ETYCCT possesses the strip-like morphology of the cotton templates, and the surfaces of its $(Ca_{0.8}Yb_{0.2})F_{2.2}$ cores are loaded with many anatase nanoparticles and rutile nanorods. The NIR ($\lambda \geq$ 780 nm) driven degradation rate of MO over C-ETYCCT is 52.34% after 180 min, which is 1.6 and 2.5 times as high as those of C-ETYCT and C-ETYCC, respectively. Under UV−vis−NIR light irradiation for 10 min, the degradation rates of MO and SA over C-ETYCCT are 90.25 and 78.79%, respectively, apparently higher than those of C-ETYCT and C-ETYCC.

■ ASSOCIATED CONTENT

Supporting Information

The Supporting Information is available free of charge on the ACS Publications website at DOI: 10.1021/acsami.5b05557.

Additional figures and table as mentioned in the text. (PDF)

■ AUTHOR INFORMATION

Corresponding Author

*E-mail: liangli117@sjtu.edu.cn. Fax: +86 21 54747567. Tel: +86 21 54747567.

Author Contributions

The manuscript was written through contributions of all authors. All authors have given approval to the final version of the manuscript.

Notes

The authors declare no competing financial interest.

■ ACKNOWLEDGMENTS

This work was supported by the Science and Technology Commission of Shanghai Municipality (no. 14DZ1207306), Shanghai Rising-Star Program (no. 14QA1402400), National Natural Science Foundation of China (NSFC 21271179), and Program for New Century Excellent Talents (NCET-13-0364).

■ ABBREVIATIONS

NIR	near-infrared
C-$CaTiO_3$	cotton-templated $CaTiO_3$ semiconduction precursors
C-ETYCCT	$Er^{3+}/Tm^{3+}/Yb^{3+}$-($CaTiO_3/CaF_2/TiO_2$)

DOI: 10.1021/acsami.5b05557
ACS Appl. Mater. Interfaces 2015, 7, 20170−20178

C-ETYCT	$Er^{3+}/Tm^{3+}/Yb^{3+}$-($CaTiO_3/TiO_2$)
C-ETYCC	$Er^{3+}/Tm^{3+}/Yb^{3+}$-($CaTiO_3/CaF_2$)
C-ETYC	$Er^{3+}/Tm^{3+}/Yb^{3+}$-$CaTiO_3$
$C\text{-}ET_{(0.5-8.0\%)}YCCT_{(15-30\%)}$	$Er^{3+}/Tm^{3+}{}_{(0.5-8.0\%)}/Yb^{3+}$–($CaTiO_3/CaF_2/TiO_{2(15-30\%)}$)
TTIP	titanium isopropoxide
UV	ultraviolet
MO	methyl orange
SA	salicylic acid
XRD	X-ray diffraction
SEM	scanning electron microscopy
EDS	energy-dispersive spectroscopy
TEM	transmission electron microscopy
HRTEM	high-resolution TEM
XPS	X-ray photoelectron spectroscopy
UV–vis–NIR	ultraviolet–visible–near infrared
ESR	electron spin resonance
TOC	total organic carbon
COD	chemical oxygen demand
EEM	excitation–emission matrix

REFERENCES

(1) Tang, Y. N.; Di, W. H.; Zhai, X. S.; Yang, R. Y.; Qin, W. P. NIR-Responsive Photocatalytic Activity and Mechanism of $NaYF_4$:Yb,Tm@TiO_2 Core-Shell Nanoparticles. *ACS Catal.* **2013**, *3*, 405–412.

(2) Wang, W.; Huang, W. J.; Ni, Y. R.; Lu, C. H.; Xu, Z. Z. Different Upconversion Properties of β-$NaYF_4$: Yb^{3+}, Tm^{3+}/Er^{3+} in Affecting the Near-Infrared-Driven Photocatalytic Activity of High-Reactive TiO_2. *ACS Appl. Mater. Interfaces* **2014**, *6*, 340–348.

(3) Guo, X. Y.; Song, W. Y.; Chen, C. F.; Di, W. H.; Qin, W. P. Near-Infrared Photocatalysis of β-$NaYF_4$: Yb^{3+},Tm^{3+}@ZnO Composites. *Phys. Chem. Chem. Phys.* **2013**, *15*, 14681–14688.

(4) Li, C. H.; Wang, F.; Zhu, J.; Yu, J. C. $NaYF_4$:Yb, Tm/CdS Composite as a Novel Near-Infrared-Driven Photocatalyst. *Appl. Catal., B* **2010**, *100*, 433–439.

(5) Qin, W. P.; Zhang, D. S.; Zhao, D.; Wang, L. L.; Zheng, K. Z. Near-Infrared Photocatalysis Based on YF_3: Yb^{3+}, Tm^{3+}/TiO_2 Core-Shell Nanoparticles. *Chem. Commun.* **2010**, *46*, 2304–2306.

(6) Li, Z. Q.; Li, C. L.; Mei, Y. Y.; Wang, L. M.; Du, G. H.; Xiong, Y. J. Synthesis of Rhombic Hierarchical YF_3 Nanocrystals and Their Use as Upconversion Photocatalysts after TiO_2 Coating. *Nanoscale* **2013**, *5*, 3030–3036.

(7) Guo, X. Y.; Di, W. H.; Chen, C. F.; Liu, C. X.; Wang, X.; Qin, W. P. Enhanced Near-Infrared Photocatalysis of $NaYF_4$:Yb,Tm/CdS/TiO_2 Composites. *Dalton Trans.* **2014**, *43*, 1048–1054.

(8) Su, L. T.; Karuturi, S. K.; Luo, J.; Liu, L.; Liu, X.; Guo, J.; Sum, T. C.; Deng, R.; Fan, H.; Liu, X.; Tok, A. I. Y. Photon Upconversion in Hetero-nanostructured Photoanodes for Enhanced Near-Infrared Light Harvesting. *Adv. Mater.* **2013**, *25*, 1603–1607.

(9) Huang, S. Q.; Lou, Z. Y.; Shan, A. D.; Zhu, N. W.; Feng, K. L.; Yuan, H. P. An Efficient Near Infrared Photocatalyst of $Er^{3+}/Tm^{3+}/Yb^{3+}$ Tridoped ($CaWO_4$@(TiO_2/CaF_2)) with Multi-Stage CaF_2 Nanocrystal Formation. *J. Mater. Chem. A* **2014**, *2*, 16165–16174.

(10) Mizoguchi, H.; Ueda, K.; Orita, M.; Moon, S. C.; Kajihara, K.; Hirano, M.; Hosono, H. Decomposition of Water by a $CaTiO_3$ Photocatalyst under UV Light Irradiation. *Mater. Res. Bull.* **2002**, *37*, 2401–2406.

(11) Zhang, H.; Chen, G.; Li, Y.; Teng, Y. Electronic Structure and Photocatalytic Properties of Copper-Doped $CaTiO_3$. *Int. J. Hydrogen Energy* **2010**, *35*, 2713–2716.

(12) Su, B. T.; Wang, K.; Dong, N.; Mu, H. M.; Lei, Z. Q.; Tong, Y. C.; Bai, J. Biomorphic Synthesis of Long ZnO Hollow Fibers with Porous Walls. *J. Mater. Process. Technol.* **2009**, *209*, 4088–4092.

(13) Xiao, G.; Huang, X.; Liao, X.; Shi, B. One-Pot Facile Synthesis of Cerium-Doped TiO_2 Mesoporous Nanofibers Using Collagen Fiber as the Biotemplate and Its Application in Visible Light Photocatalysis. *J. Phys. Chem. C* **2013**, *117*, 9739–9746.

(14) Huang, S. Q.; Lou, Z. Y.; Qi, Z. B.; Zhu, N. W.; Yuan, H. P. Enhancing Upconversion Emissions of $Er^{3+}/Tm^{3+}/Yb^{3+}$ Tridoped ($NaY(WO_4)_2/YF_3$) Through TiO_2 Coating and Bi^{3+} Doping and Its Photocatalytic Applications. *Appl. Catal., B* **2015**, *168–169*, 313–321.

(15) Nilges, M. J.; Pan, Y. M.; Mashkovtsev, R. I. Radiation-Damage-Induced Defects in Quartz. I. Single-Crystal W-Band EPR Study of Hole Centers in an Electron-Irradiated Quartz. *Phys. Chem. Miner.* **2008**, *35*, 103–115.

(16) Antcliff, K. L.; Murphy, D. M.; Griffiths, E.; Giamello, E. The Interaction of H_2O_2 with Exchanged Titanium Oxide Systems (TS-1, TiO_2, [Ti]-APO-5, Ti-ZSM-5). *Phys. Chem. Chem. Phys.* **2003**, *5*, 4306–4316.

(17) Ji, H. H.; Chang, F.; Hu, X. F.; Qin, W.; Shen, J. W. Photocatalytic Degradation of 2,4,6-Trichlorophenol Over g-C_3N_4 under Visible Light Irradiation. *Chem. Eng. J.* **2013**, *218*, 183–190.

(18) Canevali, C.; Chiodini, N.; Morazzoni, F.; Scotti, R. Electron Paramagnetic Resonance Characterization of Ruthenium-Dispersed Tin Oxide Obtained by Sol–Gel and Impregnation Methods. *J. Mater. Chem.* **2000**, *10*, 773–778.

(19) Sobana, N.; Muruganadham, M.; Swaminathan, M. Nano-Ag Particles Doped TiO_2 for Efficient Photodegradation of Direct Azo Dyes. *J. Mol. Catal. A: Chem.* **2006**, *258*, 124–132.

(20) Wei, L. H.; Wu, S. Y.; Zhang, Z. H.; Wang, X. F.; Hu, Y. X. Investigations on the Local Structure and g Factors for the Interstitial Ti^{3+} in TiO_2. *Pramana* **2008**, *71*, 167–173.

(21) Liu, N.; Schneider, C.; Freitag, D.; Hartmann, M.; Venkatesan, U.; Müller, J.; Spiecker, E.; Schmuki, P. Black TiO_2 Nanotubes: Cocatalyst-Free Open-Circuit Hydrogen Generation. *Nano Lett.* **2014**, *14*, 3309–3313.

(22) Zuo, F.; Wang, L.; Wu, T.; Zhang, Z. Y.; Borchardt, D.; Feng, P. Y. Self-Doped Ti^{3+} Enhanced Photocatalyst for Hydrogen Production under Visible Light. *J. Am. Chem. Soc.* **2010**, *132*, 11856–11857.

(23) Chen, W.; Westerhoff, P.; Leenheer, J. A.; Booksh, K. Fluorescence Excitation-Emission Matrix Regional Integration to Quantify Spectra for Dissolved Organic Matter. *Environ. Sci. Technol.* **2003**, *37*, 5701–5710.

(24) De Laurentiis, E.; Maurino, V.; Minero, C.; Vione, D.; Mailhot, G.; Brigante, M. Could Triplet-Sensitised Transformation of Phenolic Compounds Represent a Source of Fulvic-Like Substances in Natural Waters? *Chemosphere* **2013**, *90*, 881–884.

(25) Her, N.; Amy, G.; Chung, J.; Yoon, J.; Yoon, Y. Characterizing Dissolved Organic Matter and Evaluating Associated Nanofiltration Membrane Fouling. *Chemosphere* **2008**, *70*, 495–502.

(26) Coble, P. G. Characterization of Marine and Terrestrial DOM in Seawater Using Excitation-Emission Matrix Spectroscopy. *Mar. Chem.* **1996**, *51*, 325–346.

DOI: 10.1021/acsami.5b05557
ACS Appl. Mater. Interfaces 2015, 7, 20170–20178